Common-Mode Differential-Mode (CMDM) Method for Double-Nuclear MR Signal Excitation and Reception at Ultrahigh Fields

Yong Pang,
Department of Radiology and Biomedical Imaging, University of California San Francisco, San Francisco, CA 94158 USA

Xiaoliang Zhang,
Department of Radiology and Biomedical Imaging, University of California San Francisco, San Francisco, CA 94158 USA, and with UCSF/UC Berkeley Joint Graduate Group in Bioengineering, San Francisco, CA 94720 USA, and also with the California Institute for Quantitative Biosciences (QB3), San Francisco, CA 94158 USA

Zhentian Xie,
Department of Radiology and Biomedical Imaging, University of California San Francisco, San Francisco, CA 94158 USA

Chunsheng Wang, and
Department of Radiology and Biomedical Imaging, University of California San Francisco, San Francisco, CA 94158 USA

Daniel. B. Vigneron
Department of Radiology and Biomedical Imaging, University of California San Francisco, San Francisco, CA 94158 USA, and with UCSF/UC Berkeley Joint Graduate Group in Bioengineering, San Francisco, CA 94720 USA, and also with the California Institute for Quantitative Biosciences (QB3), San Francisco, CA 94158 USA

Xiaoliang Zhang: xlzhang@berkeley.edu

Abstract

Double-tuned radio-frequency (RF) coils for heteronuclear mangentic resonance (MR) require sufficient electromagnetic isolation between the two resonators operating at two Larmor frequencies and independent tuning in order to attain highly efficient signal acquisition at each frequency. In this work, a novel method for double-tuned coil design at 7T based on the concept of common-mode differential-mode (CMDM) was developed and tested. Common mode (CM) and differential mode (DM) currents exist within two coupled parallel transmission lines, e.g., microstrip lines, yielding two different current distributions. The electromagnetic (EM) fields of the CM and DM are orthogonal to each other, and thus, the two modes are intrinsically EM decoupled. The modes can be tuned independently to desired frequencies, thus satisfying the requirement of dual-frequency MR applications. To demonstrate the feasibility and efficiency of the proposed CMDM technique, CMDM surface coils and volume coils using microstrip transmission line for ^1H and ^{13}C MRI/MRSI were designed, constructed, and tested at 7T. Bench test results showed that the isolations between the two frequency channels of the CMDM surface coil and volume coil were better than −30 and −25 dB, respectively. High quality MR phantom images were also obtained using the CMDM coils. The performance of the CMDM technique was

validated through a comparison with the conventional two-pole design method at 7T. The proposed CMDM technique can be also implemented by using other coil techniques such as lumped element method, and can be applied to designing double-tuned parallel imaging coil arrays. Furthermore, if the two resonant modes of a CMDM coil were tuned to the same frequency, the CMDM coil becomes a quadrature coil due to the intrinsic orthogonal field distribution of CM and DM.

Index Terms

Double-tuned coil; common-mode differential-mode (CMDM); high field; magnetic resonance imaging (MRI); parallel imaging transceiver array

I. Introduction

Heteronuclear (e.g., ^{31}P [1]–[9], ^{13}C [8], [10]–[17], ^{23}Na [18]–[25], ^{19}F [26], [27], and ^{17}O [28]–[30]) MR spectroscopy and spectroscopic imaging has been playing an important role in investigation of metabolism and physiological changes *in vivo*. Heteronuclear MRS/MRSI has been widely used for noninvasive studies of bioenergetics [6], [8], [9], metabolism [1]–[3], [7], [10], [11], [13], [16], stroke [25], myocardial infarction [4] and cellular physiology [12], [17], drug dynamics and delivery [5], [26], [27] and direct detection of cerebral metabolic rate of oxygen [28]–[30]. However, the low sensitivity of the heteronuclei (mainly due to their low natural abundance) significantly limits performance, especially for *in vivo* applications. With the advent of ultrahigh field MR [31]–[36] and commercial hyperpolarizers, sensitivity of heteronuclear MR can be significantly improved, resulting in greatly improved noninvasive imaging tools for biomedical research with both higher spatial resolution and higher temporal resolution than previously. In particular, by using the ^{13}C hyperpolarization methods with > 50 000 fold sensitivity enhancement *in vivo* [37]–[41], it becomes possible to observe key cellular bioenergetic processes *in vivo* by ^{13}C MR. A major challenge of implementing heteronuclear MRS/MRSI, particularly at ultrahigh fields, is the design of efficient double-tuned radio-frequency (RF) coils [42]–[49] to optimally detect subtle MR signals from heteronuclei. Heteronuclear MR requires double-tuned RF coils which operate at usually proton Larmor frequency and the lower heteronucleus Larmor frequency. In such double-tuned RF coils, the proton channel is necessary for performing B_0 shimming and anatomic image acquisitions which would be used for correlating the metabolic information collected using the heteronuclear channel. For *in vivo* heteronuclear MR studies, it is essential for the double-tuned RF coils to have sufficient electromagnetic isolation between the two channels and independent tuning at each frequency, in addition to high quality factors (*Q*-factors), so that highly efficient acquisitions can be attained. The cross-talk between the two channels is one of the major factors that degrade the capability of detection of the already small signal intensity of heteronuclei *in vivo*, ultimately reducing the MR sensitivity and thus imaging resolution. The two-pole circuit method is one of important techniques for double-tuned RF coil designs [43]. This method is easy to implement and is particularly suitable for double-tuned surface coil designs. The two-pole circuit is also used to design resonant elements in double-tuned volume coils [50]. Trap circuits [48], [49] and 4-ring schemes [46] have been proposed for double-tuned operation of birdcage type volume coils. The technique of alternately positioning proton and heteronuclear elements has also been employed in designing double-tuned volume coils [47], [51].

In this work, we propose a new method using the common-mode and differential-mode (CMDM) technique to design double-tuned RF coils for heteronuclear MR applications. In a resonator that supports common mode (CM) and differential mode (DM), the EM fields of

the two modes are orthogonal to each other and are intrinsically EM decoupled [52], [53]. The resonant frequencies of the common mode and the differential mode can be controlled independently and tuned to the desired values to satisfy the requirement of heteronuclear MR applications. The CMDM resonators can be realized by using many different approaches, such as lumped elements and transmission lines. To validate the proposed CMDM design method, double-tuned CMDM surface coils and volume coils were designed and constructed for $^{13}C/^1H$ MR applications at 7T. All the CMDM coils in this work were realized by using microstrip transmission line method which has been proven to be advantageous for ultrahigh field RF coil designs with high frequency operation capability, high quality factor, reduced radiation losses and improved MR sensitivity [54]–[62]. The resonant frequencies and B_1 field distributions of the double-tuned CMDM surface coils and volume coils at 7T were numerically analyzed using the finite difference time domain (FDTD) algorithm [63]–[66]. Proton images and ^{13}C spectroscopic images of a phantom were acquired using the double-tuned CMDM surface coil and volume coil at 7T to investigate the feasibility of the proposed CMDM method for designing double-tuned RF coils for heteronuclear MR applications.

II. Materials and Methods

A. Microstrip CMDM Surface Coil Design

Prior to building the CMDM surface coil, we established a model to numerically analyze the CMDM structure by using the finite-difference time-domain (FDTD) algorithm in terms of the reflection coefficient S_{11}, the transmission coefficient S_{12}, and the resonant frequencies and the magnetic field distributions of the CM and DM. Based on the FDTD simulation results on the capacitance of the termination capacitors, the resonator dimensions and the substrate thickness, the double-tuned CMDM surface coil was designed and constructed for 7T. Bench tests and MR experiments were conducted to fine tune the coil and evaluate its performance.

In the simulation, the software XFDTD 6.4 (Remcom, State College, PA) was used to build the model of the double-tuned CMDM surface coil shown in Fig. 1 and to perform all the FDTD numerical calculations. The CMDM coil was modeled as an 89-mm-long and 32-mm-wide split microstrip resonator. The permittivity of the substrate of the microstrip CMDM resonator was set to 2.62, which is the permittivity of the acrylic board used in building the prototypes. The strip conductor with a width of 6.3 mm and ground plane were modeled as a thin copper foil. The two ends of the strip conductor were connected through a variable capacitor (i.e., C_3 in Fig. 1) to support the differential mode. By connecting termination capacitors (i.e., C_1 and C_2 in Fig. 1) at both ends of the microstrip conductors using perfect electric conductors, a CM microstrip resonator with capacitive termination was formed. Besides using the numerical calculation method, the resonant frequency of the common mode of the CMDM coil can also be estimated by using the following analytic equation [57]:

$$f_{re} = \frac{(2\pi f_{re} Z_0)^2 C_1 C_2 - 1}{2\pi Z_0 (C_1 + C_2)} \tan\left(\frac{2\pi l \sqrt{\varepsilon_{eff}}}{c} f_{re}\right) \quad (1)$$

where C_1 and C_2 are the capacitances of the termination capacitors on the microstrip resonator as indicated in Fig. 1. l and ε_{eff} are the length and effective permittivity of the microstrip resonator. Z_0 is the characteristic impedance of the microstrip resonator. In practice, the frequency tuning for the common mode can be performed by adjusting C_1 and C_2 through variable capacitors.

The coaxial cables for feeding both the CM and DM coils was modeled as a series voltage source with 50 Ω impedance which was connected to each driven port of the CMDM coil. The cell size used for FDTD mesh was 1 mm, which was small enough for satisfying the simulation accuracy. By changing the capacitor values the common mode and differential mode were tuned to ^{1}H and ^{13}C Larmor frequencies at 7T, respectively.

The proposed double-tuned CMDM surface coil was built on a 6.3-mm-thick acrylic board which served as both dielectric substrate and mechanical support. In this microstrip type CMDM surface coil, the strip conductors and the ground planes were made from back-adhesive copper foils (3M, St. Paul, MN). The dimensions of the CMDM surface coil were the same as those used in the simulation setup. To reach the desired resonant frequency for common mode, one end of the CMDM coil was terminated by a variable capacitor (NMAF19HV, Voltronics, Denville, NJ) ranging from 1 to 19 pF which was also used for frequency tuning. Another end of the CMDM coil was terminated by two fixed capacitors with nominal value of 24 pF (ATC, Huntington Station, NY). For the differential mode, a fixed capacitor with nominal value of 30 pF (ATC, Huntington Station, NY) and a variable capacitor (9629, Johanson MFG, Boonton, NJ) ranging from 5 to 20 pF were connected in parallel in the gap of the CMDM coil.

In this study, the common mode and differential mode were driven capacitively and inductively, respectively, as shown in Fig. 1. A variable capacitor (NMAF19HV, Voltronics, Denville, NJ) with a capacitance range from 1 to 19 pF was connected in series to the CMDM microstrip coil to implement impedance match for the common mode. The differential mode was fed by an inductive loop with a variable capacitor (9629, Johanson MFG, Boonton, NJ) ranging from 5 to 20 pF used for impedance match. Bench tests on the coil resonance modes and the isolation between the CM and DM channels were performed by reflection coefficient S_{11} and transmission coefficient S_{21} measurements taken on an Agilent E5070B network analyzer.

MR experiments were also conducted to validate the performance of this double-tuned CMDM coil. The ^{1}H MR imaging and ^{13}C spectroscopic imaging experiments of a cylindrical corn oil phantom were performed on a GE 7T whole body MR system (GE Healthcare, Waukesha, WI). For ^{1}H imaging, the common mode of the CMDM coil was used to collect a set of spin echo (SE) images in axial plane with imaging parameters of TR = 2 s FOV = 9 cm, and number of averages = 1. In the ^{13}C spectroscopy experiment, the differential mode of the CMDM coil was used to acquire a set of 16 × 8 2-D ^{13}C FIDCSI data with acquisition parameters of TR = 2 s, in-plane resolution = 9 mm × 9 mm slice thickness = 20 mm, and number of averages = 1.

To further validate the CMDM method for double-tuned coil design, we built a conventional double-tuned RF coil based on the two-pole circuit [43] as shown in Fig. 2, and compared it with the proposed CMDM coil in terms of Q-values, isolation between ^{13}C and ^{1}H channels, transmit efficiency and SNR at 7T. The conventional double-tuned two-pole coil was built with the same size as the CMDM coil: the coil was in rectangular shape with dimensions of 89 mm 32 mm. The width of the copper tape used as coil conductors was 6.3 mm. This two-pole circuit was built on a 6.3-mm-thick acrylic board in order to keep the same as what used in the CMDM design. A piece of adhesive backed copper foil (3M, St. Paul, MN) was placed on the other side of the acrylic board to act as the RF shielding. Both bench measurements and MR experiments were performed using the CMDM coil and the two-pole coil with the same parameters and setup. Importantly, the distance between the coil and the sample (water phantom) was kept same during all imaging experiments and bench measurements. The imaging parameters used for the comparison study were as following: pulse sequence = fast gradient echo FOV = 10 cm, slice thickness = 3 mm, slice spacing = 5

mm, TE/TR = 2.2/200 ms, number of averages = 1, matrix size = 128 × 128, and flip angle = 30°.

B. Microstrip CMDM Volume Coil Design

Based on the structure of the CMDM surface coil described above, we built a double-tuned CMDM volume coil for ^{1}H/^{13}C *in vivo* MR applications at 7T (as shown in Fig. 3) to demonstrate the capability of CMDM technique in designing double-tuned volume coils. An acrylic cylinder with dimensions of 102 mm OD, 95 mm ID, and 102 mm in length was utilized as the dielectric material and mechanical support. This double-tuned CMDM volume coil comprised of eight identical CMDM resonator elements equally spaced along the circumference of the acrylic cylinder with a 1.6-mm separation. The circuit structure of each element was the same as that of the CMDM surface coil described above, but the dimensions of the rectangular element were changed to 102 mm in length and 36 mm in width. In this double-tuned CMDM volume coil, the common mode and differential mode of each element were used to form the volume coil's ^{1}H channel and ^{13}C channel, respectively. The ground plane of the coil was made of a cylindrical copper foil with 36 μm thickness (3M, St. Paul, Minnesota) on the outer surface of the acrylic cylinder. This continuous ground plane can effectively enhance the coupling among the CMDM microstrip elements and reduce radiation losses [67].

The resonant frequency f_{vc} of the CMDM volume coil can be calculated by using the following equation [57]:

$$f_{ve} = \frac{1}{\sqrt{1 + \frac{1}{L}\sum_{i=1}^{N-1} k_{1,i+1}\cos\left(\frac{2\pi}{N}i\right)}} f_{re} \quad (2)$$

where $k_{1,\ i+1}$ is the mutual inductance between the first element and the $(i+1)$ th elements; f_{re} denotes the resonant frequency of CM or DM for each CMDM element; N is the number of elements for the volume coil. In this CMDM volume coil design, the magnetic coupling dominated the coupling between the elements, therefore the electric coupling was ignored and only mutual inductance induced voltage from the other resonant elements was considered for the frequency calculation. From (2), it can be seen that the resonant frequency of the volume coil is slightly lower than that of each element due to the mutual coupling among elements.

As in the CMDM surface coil, the ^{1}H channel of volume coils was driven capacitively and ^{13}C channel was driven inductively. To generate circularly polarized B_1 fields, the coil was operated in quadrature driving for both the ^{1}H and ^{13}C channels. In each channel, the two driving elements of the volume coil were 90° apart and fed with a 90° difference in phase.

A network analyzer (Agilent E5070B) was employed for testing the coil resonance modes and performance, including Q-factors and the electromagnetic isolations between the two quadrature ports and also between ^{1}H and ^{13}C channels.

After the bench tests and fine tuning, ^{1}H MR imaging and ^{13}C spectroscopy experiments of a cylindrical corn oil phantom were performed by using the CMDM volume coil with a cylindrical corn oil phantom on the GE 7T whole body MR scanner. A set of fast spin echo (FSE) images in both sagittal and axial planes were acquired with imaging parameters of TR = 2 s, TE = 24 ms, flip angle FA = 90° slice thickness = 5 mm and number of average = 1. An 8 × 8 2-D ^{13}C spectroscopic image was also obtained using a FIDCSI sequence with TR = 2 s, number of average = 4, 12 mm in plane and 20-mm-thick slice.

C. Evaluation of B_1 Field Behavior and Performance of the CMDM Structures

The structure of split microstrip resonators that supports common mode and differential mode is different from that of the typical microstrip resonators. To investigate the B_1 field distributions of a double-tuned CMDM volume coil at both frequencies, we did studies using both numerical simulation and MR imaging experiments. In the simulation, we built a numerical model which was exactly the same as the prototype CMDM volume coil described above, and then used the FDTD method to calculate and analyze the B_1 field distribution of both channels. A cylindrical human muscle phantom with permittivity of 58 and conductivity of 0.8 (S/m) was placed in the CMDM volume coil model. The diameter of the phantom was 61 mm which was about 63% of the coil ID. The B_1 field distributions in both axial and sagittal planes were simulated. The standard deviation of B_1 intensity was utilized to quantitatively evaluate the B_1 homogeneity within the phantom area.

The Yee cell size was 1 mm on transverse plane and 3 mm on longitudinal direction and was small enough to satisfy the calculation accuracy. To simulate the B_1 field distribution of the CMDM volume coil model when operating with common mode, current source was placed at the point of C1 (in Fig. 1) for each CMDM resonator and the phase difference between the adjacent elements was 45°. In the simulation of differential mode, the current source was placed at point C3 shown in Fig. 1 for each CMDM resonator and the phase difference between adjacent elements was also 45°. This setting would make the volume coil working at sinusoidal mode to generate homogeneous B_1 field at both frequencies. The stop criteria were that the convergence reached −60 dB or the time period reached 70 cycles which ensured the achievement of the steady state.

In the MR imaging validation, a corn oil phantom was used because it contains both ^{1}H and ^{13}C and also because it has a low permittivity that can avoid the image inhomogeneity problem caused by the "dielectric resonance" effect at ultrahigh fields and can provide the more accurate information on intrinsic B_1 field distributions of the CMDM volume coil. The imaging acquisitions were performed on the General Electric (GE) whole body 7T scanner. With a fast spin echo sequence, ^{1}H imaging of the cylindrical oil phantom was acquired using the common mode channel of the CMDM volume coil. Relatively long repetition time (TR) of 2 s was employed to reduce the possible saturation effect due to the longer T1 at 7T. Other imaging parameters were TE = 4 ms, flip angle = 90°. To test the ^{13}C channel, chemical shift imaging (CSI) was acquired from the same oil phantom using the differential mode channel of the CMDM volume coil. The ^{13}C CSI studies were performed to provide information on the B_1 field behavior of the differential mode.

III. Results

A. Microstrip CMDM Surface Coil Design

In the FDTD simulation, the waveform source of Gaussian function was used to find proper capacitances for double tuned CMDM microstrip surface coil based on the resonant frequency. The convergence threshold in the calculations was set to −35 dB. Capacitances for the CM working at 298.1 MHz and DM at 75 MHz were identified, which helped to guide the double-tuned CMDM surface coil design for ^{1}H/^{13}C MRSI at 7T. In calculating the B_1 fields, a Sine wave was used and the convergence threshold was set at −40 dB. Simulation results showed that both S_{11} and S_{21} were better than −46 dB, indicating an excellent impedance matching and isolation between the ^{1}H and ^{13}C channels which is essential for efficient acquisition of ^{13}C and ^{1}H signals. Fig. 4 shows the two B_1 field distributions of the common mode and differential mode of the CMDM double-tuned surface coil. The two B_1 fields are orthogonal to each other; therefore the two modes are electromagnetically decoupled intrinsically. It was observed that the common mode and differential mode of the proposed CMDM resonator had similar B_1 field distributions, which

indicates that both ^{1}H and ^{13}C channels have the similar imaging coverage in unloaded case. When the coil is loaded with a biological sample such as human brain at the ultrahigh field of 7T, the high permittivity of the sample helps improving the field penetration for the proton channel [59].

In the bench tests, the common mode and differential mode were tuned to 298.1 and 75 MHz, respectively, by adjusting the tuning capacitors on the CMDM coil. The S_{11} measurements demonstrated that the input impedance of ^{1}H and ^{13}C channels were well matched to 50Ω. The isolations between the two frequency channels was measured −30 dB or better in both unloaded and loaded cases, illustrating that the two channels of the prototype CMDM surface coil had excellent isolation for efficient ^{1}H/^{13}C MRI/MRS.

Prior to imaging acquisitions, B_0 field shimming was performed using the CM ^{1}H channel. ^{1}H spin echo images and the ^{13}C spectroscopic images in the axial plane of a corn oil phantom were then acquired using the double tuned CMDM surface coil. Both the ^{1}H image and the ^{13}C spectroscopic image shown in Fig. 5 verified that the B_1 fields of the common mode and differential mode of the CMDM surface coil have a similar distribution and coverage.

The comparison study was conducted with the proposed CMDM coil and the double-tuned two-pole coil at the field strength of 7T. The results of the bench tests on the two coils are shown in Table I. The Q-values of the CMDM coil for both ^{1}H and ^{13}C channels are higher than those of the two-pole coil. The electromagnetic isolation between the two nuclear channels in double-tuned coils is a critical factor that influences the coil efficiency. The isolation measured between the two channels of the CMDM coil reached −44 dB or better while that of the two-pole coil was −20 dB, which demonstrates the proposed CMDM coil has an improved electromagnetic isolation between two channels and thus the improved coil efficiency.

Fig. 6 shows MR imaging results of this comparison study. Proton images of a water phantom acquired using the two coils as well as their SNR measurements along the central line of each image illustrated that the proposed CMDM coil could provide an improved SNR over the conventional two-pole double-tuned coil. Quantitatively, the highest achievable SNR of the CMDM coil and the two-pole coil are 817 and 714, respectively, or a 13% improvement in this specific case. To compare the transmit efficiency of the two coils, the power was calibrated using a 7-mm-diameter water tube with 5-mm slice thickness to define the 90° pulse. The water tube was located 8 mm above the coil center. MR imaging experiments also demonstrated that the RF power required to achieve a nominal 90° flip angle using the proposed CMDM coil was approximately 20% less than that using the conventional two-pole coil, showing high transmit efficiency of the proposed CMDM design.

B. Microstrip CMDM Volume Coil Design

The ^{1}H and ^{13}C channels of the microstrip CMDM volume coil were tuned to 298.1 MHz and 75 MHz on the two quadrature ports respectively. Each port of the ^{1}H channel was matched to system 50Ω via a series capacitor. Well defined five resonance peaks for both ^{1}H and ^{13}C channels are clearly identified on the network analyzer showing a proper behavior of this 8-element volume coil in terms of resonance modes and the interaction between the two nuclear channels. On the bench test, the isolations between the quadrature driving ports of both ^{1}H and ^{13}C channels were greater than −20 dB, indicating that the driving ports of each channel have been decoupled sufficiently, meeting the requirement of the 90° phase difference between the two quadrature ports. The S_{21}-parameter between ^{1}H and ^{13}C channels was better than −30 dB, showing excellent isolation between the two nuclear

channels. This is essential to ensure the efficiency of the excitation and reception of the ^{1}H and ^{13}C MR signals.

B_0 shimming was performed by using the common mode ^{1}H channel prior to the MR imaging experiments on the 7T system. Proton imaging and ^{13}C spectroscopic imaging were acquired from the cylindrical corn oil phantom using the common mode channel and differential mode channel, respectively. Fig. 7 shows the ^{1}H FSE images in both sagittal and axial planes of the corn oil phantom, as well as a ^{13}C FIDCSI image in the same axial plane. The ^{1}H images and ^{13}C spectroscopic images of the oil phantom illustrated the homogeneous intrinsic B_1 distributions of this 7T double-tuned CMDM volume coil at both 298 MHz and 75 MHz.

C. Evaluation of B_1 Field Behavior and Performance of the CMDM Volume Coils

Fig. 8 shows the B_1 field distributions of both common mode and differential mode of the CMDM volume coil model after steady state has been achieved in FDTD simulation. The 2-D distributions of the B_1 fields in the axial plane for ^{1}H and ^{13}C are illustrated in Fig. 8(a) and (b), respectively. The black circle on the B_1 maps denotes the position of the phantom. The standard deviation and mean of the ^{1}H channel are 4.7×10^{-3} Gauss and 5.3×10^{-2} Gauss, respectively, while those for the ^{13}C channel are 6.9×10^{-4} Gauss and 5.7×10^{-2} Gauss. The ratio between the standard deviation and the mean are 9% and 1% for ^{1}H and ^{13}C channel, respectively. The 1-D plots of the B_1 field distributions along the central line are also shown in Fig. 8(c). In this CMDM volume coil, the average B_1 intensity of the common mode is approximately 7% less than that of the differential mode, while the B_1 of the common mode in the center of the phantom is 3% higher than that of the differential mode. This difference results from the different B_1 distribution of the two resonance modes. The B_1 distribution and penetration of the common mode and differential mode change with geometry and dimension of CMDM units. Both quantitative calculation and the graphic illustrations demonstrate fairly homogeneous B_1 fields in axial plane can be achieved for ^{13}C channel; while for ^{1}H channel (at a higher frequency of 298 MHz), the B_1 behaves properly although the "dielectric resonance" effect in the high permittivity biological samples at ultrahigh fields distorts B_1 the field distribution at certain level.

In Fig. 8(d)–(f), 2-D distributions and 1-D plots of B_1 fields for both ^{1}H and ^{13}C channels in sagittal planes are illustrated. The black rectangle in the B_1 maps denotes the position of the phantom. For ^{1}H channel, the standard deviation and mean of the B_1 intensity are 1.34×10^{-2} Gauss and 4.3×10^{-2} Gauss, respectively, between which the ratio is 30%; while for ^{13}C channel those are 1.0×10^{-2} Gauss and 5.2×10^{-2} Gauss respectively, between which the ratio is 20%. Based on this simulation, B_1 fields of ^{13}C channel (at a relatively lower frequency of 75 MHz) have more uniform distribution along the volume coil axis than that of ^{1}H channel which operates at an approximately 4-times higher frequency of 298 MHz.

IV. Discussion and Conclusion

All the simulations, bench tests and MR imaging experiments have demonstrated that the proposed method based on the concepts of CMDM is a feasible and effective approach to design double-tuned coils at 7T. One important advantage of the CMDM design is that its common mode and differential mode are intrinsically decoupled because their magnetic fields are orthogonal to each other. This feature is critical for improving efficiency for both proton and heteronucleus MR signal excitation and reception in dual-tuned operations. The common mode and differential mode of CMDM resonator can be tuned independently. Compared with conventional approaches, the proposed CMDM method provides an easy and robust way to double-tuned RF coil designs. In this work, although the CMDM method

is implemented by using microstrip technology in order to gain the performance at high and ultrahigh fields, the CMDM resonator can be also realized by using other type of circuits, such as lumped element designs. Moreover, if the CM and DM of a CMDM resonator are tuned to the same frequency, the CMDM coil becomes a quadrature coil due to the intrinsically orthogonal field distribution of the CM and DM. In the design of the proposed CMDM RF coils, it is important to keep circuit and structure symmetric in both electrical and mechanical aspects. Any circuit imbalance would contaminate the mode and sacrifice coil efficiency, particularly in quadrature CMDM case where the common mode and differential mode operate at the same frequency.

The FDTD simulation of the CMDM double-tuned single surface coil showed that its CM and DM possess a similar B_1 distribution. This indicates that the CM and DM coils have almost the same imaging coverage in the unloaded case. In the loaded case with a high permittivity biological sample at the ultrahigh field of 7T, the RF field penetration is increased due to the "dielectric resonance" effect. This guarantees the imaging coverage of proton channel to not be smaller than that in the unloaded case. In addition, this characteristic may help the B_0 shimming for heteronuclei, e.g., ^{13}C, whose spin density is normally too low in human body to generate strong enough MR signals for shimming. Commonly, ^{1}H channel is used for B_0 shimming in double-tuned coils, which requires a similar magnetic field distribution for two frequency channels. The similar or same field distribution may help improving the shimming efficiency.

The concepts of CMDM RF coil design have been demonstrated in designing regular surface coils and volume coils. Potentially the proposed CMDM method can also be used to design double-tuned coil arrays or double-tuned transceiver arrays for parallel imaging or parallel excitation applications. The decoupling issue of the CMDM arrays can be addressed by employing the magnetic wall technique which is suitable for non-overlapped coil array designs and which also shows the unique advantage in double-tuned arrays [68], [69]. It is known that non-overlapped array can decrease the g-factor and increase the SNR, therefore it is desired in parallel imaging and parallel excitation applications.

Acknowledgments

References

1. Ackerman JJH, Grove TH, Wong GG, Gadian DG, Radda GK. Mapping of metabolites in whole animals by ^{31}P NMR using surface coils. Nature. 1980; 283:167–170. [PubMed: 7350541]

2. Bottomley PA, Cousins JP, Pendrey DL, Wagle WA, Hardy CJ, Eames FA, McCaffrey RJ, Thompson DA. Alzheimer dementia: Quantification of energy metabolism and mobile phosphoesters with P-31 NMR spectroscopy. Radiology. 1992; 183:695–699. [PubMed: 1584923]

3. Chatham JC, Blackband SJ. 31P chemical shift imaging of the regionally ischemic perfused heart. NMR Biomed. 1990; 3:190–193. [PubMed: 2206851]

4. Hetherington HP, Luney DJ, Vaughan JT, Pan JW, Ponder SL, Tschendel O, Twieg DB, Pohost GM. 3D 31P spectroscopic imaging of the human heart at 4.1 T. Magn Reson Med. 1995; 33:427–431. [PubMed: 7760712]

5. Kaplan O, van Zijl PC, Cohen JS. Information from combined 1H and 31P NMR studies of cell extracts: Differences in metabolism between drug-sensitive and drug-resistant MCF-7 human breast cancer cells. Biochem Biophys Res Commun. 1990; 169:383–390. [PubMed: 2357212]

6. Lei H, Zhu XH, Zhang XL, Ugurbil K, Chen W. In vivo 31P magnetic resonance spectroscopy of human brain at 7 T: An initial experience. Magn Reson Med. 2003; 49:199–205. [PubMed: 12541238]

7. Moonen CT, van Zijl PC, Le Bihan D, DesPres D. In vivo NMR diffusion spectroscopy: 31P application to phosphorus metabolites in muscle. Magn Reson Med. 1990; 13:467–477. [PubMed: 2325547]

8. Shulman RG, Brown TR, Ugurbil K, Ogawa S, Cohen SM, den Hollander JA. Cellular applications of 31P and 13C nuclear magnetic resonance. Science. 1979; 205:160–166. [PubMed: 36664]

9. Ugurbil K, Rottenberg H, Glynn P, Shulman RG. 31P nuclear magnetic resonance studies of bioenergetics and glycolysis in anaerobic Escherichia coli cells," in. Proc Natl Acad Sci U S A. 1978; 75:2244–2248. [PubMed: 27785]

10. Bottomley PA, Hardy CJ, Roemer PB, Mueller OM. Proton-decoupled, overhauser-enhanced, spatially localized carbon-13 spectroscopy in humans. Magn Reson Med. 1989; 12:348–363. [PubMed: 2560801]

11. Chen W, Adriany G, Zhu XH, Gruetter R, Ugurbil K. Detecting natural abundance carbon signal of NAA metabolite within 12-cm3 localized volume of human brain using 1H-[13C] NMR spectroscopy. Magn Reson Med. 1998; 40:180–184. [PubMed: 9702699]

12. Choi IY, Tkac I, Ugurbil K, Gruetter R. Noninvasive measurements of [1-(13C)]glycogen concentrations and metabolism in rat brain in vivo. J Neurochem. 1999; 73:1300–1308. [PubMed: 10461925]

13. Gruetter R, Adriany G, Choi IY, Henry PG, Lei H, Oz G. Localized in vivo 13C NMR spectroscopy of the brain. NMR Biomed. 2003; 16:313–338. [PubMed: 14679498]

14. Hyder F, Brown P, Nixon TW, Behar KL. Mapping cerebral glutamate 13C turnover and oxygen consumption by in vivo NMR. Adv Exp Med Biol. 2003; 530:29–39. [PubMed: 14562702]

15. Laughlin MR, Taylor J, Chesnick AS, DeGroot M, Balaban RS. Pyruvate and lactate metabolism in the in vivo dog heart. Am J Physiol. 1993; 264:H2068–H2079. [PubMed: 8322935]

16. Shen J, Petersen KF, Behar KL, Brown P, Nixon TW, Mason GF, Petroff OA, Shulman GI, Shulman RG, Rothman DL. Determination of the rate of the glutamate/glutamine cycle in the human brain by in vivo 13C NMR," in. Proc Natl Acad Sci U S A. 1999; 96:8235–8240. [PubMed: 10393978]

17. Shulman RG, Rothman DL. 13C NMR of intermediary metabolism: Implications for systemic physiology. Annu Rev Physiol. 2001; 63:15–48. [PubMed: 11181947]

18. Boada FE, Christensen JD, Huang-Hellinger FR, Reese TG, Thulborn KR. Quantitative in vivo tissue sodium concentration maps: The effects of biexponential relaxation. Magn Reson Med. 1994; 32:219–223. [PubMed: 7968444]

19. Boehmer JP, Metz KR, Mao JT, Briggs RW. Spatial mapping of 23Na NMR signals by two-dimensional rotating frame imaging. Magn Reson Med. 1990; 16:335–341. [PubMed: 2266851]

20. Kolodny NH, Gragoudas ES, D'Amico DJ, Kohler SJ, Seddon JM, Murphy EJ, Yun C, Albert DM. Proton and sodium 23 magnetic resonance imaging of human ocular tissues. A model study. Arch Ophthalmol. 1987; 105:1532–1536. [PubMed: 2823760]

21. Kundel HL, Shetty A, Joseph PM, Summers RM, Kassab EA, Moore B. Sodium NMR imaging of lung water in rats. Magn Reson Med. 1988; 6:381–389. [PubMed: 3380000]

22. Lee SW, Hilal SK, Cho ZH. A multinuclear magnetic resonance imaging technique—Simultaneous proton and sodium imaging. Magn Reson Imaging. 1986; 4:343–350. [PubMed: 2823046]

23. Nishimura T, Sada M, Sasaki H, Yamada N, Yamada Y, Yutani C, Amemiya H, Fujita T, Akutsu T, Manabe H. Sodium nuclear magnetic resonance imaging of acute cardiac rejection in heterotopic heart transplantation. Kaku Igaku. 1987; 24:1741–1748. [PubMed: 3329255]

24. Ra JB, Hilal SK, Oh CH, Mun IK. In vivo magnetic resonance imaging of sodium in the human body. Magn Reson Med. 1988; 7:11–22. [PubMed: 3386516]

25. Thulborn KR, Boada FE, Chang SY, Davis D, Gillen JS, Noll DC, Shen GX, Talagala SL, Zhou XJ. Proton, sodium and functional MRI and proton MRS at 1.5 and 3.0 tesla," in. Proc 3rd Annu Meeting ISMRM. 1995:306.

26. Evelhoch JL. In vivo 19F nuclear magnetic resonance spectroscopy: A potential monitor of 5-fluorouracil pharmacokinetics and metabolism. Invest New Drugs. 1989; 7:5–12. [PubMed: 2661482]

27. Martino R, Malet-Martino M, Gilard V. Fluorine nuclear magnetic resonance, a privileged tool for metabolic studies of fluoropyrimidine drugs. Curr Drug Metab. 2000; 1:271–303. [PubMed: 11465049]

28. Fiat D, Ligeti L, Lyon RC, Ruttner Z, Pekar J, Moonen CT, McLaughlin AC. In vivo 17O NMR study of rat brain during 17O2 inhalation. Magn Reson Med. 1992; 24:370–374. [PubMed: 1569875]

29. Pekar J, Ligeti L, Ruttner Z, Lyon RC, Sinnwell TM, van Gelderen P, Fiat D, Moonen CT, McLaughlin AC. In vivo measurement of cerebral oxygen consumption and blood flow using 17O magnetic resonance imaging. Magn Reson Med. 1991; 21:313–319. [PubMed: 1745131]

30. Zhu XH, Zhang Y, Tian RX, Lei H, Zhang N, Zhang X, Merkle H, Ugurbil K, Chen W. Development of (17)O NMR approach for fast imaging of cerebral metabolic rate of oxygen in rat brain at high field," in. Proc Natl Acad Sci U S A. 2002; 99:13194–13199. [PubMed: 12242341]

31. Vaughan JT, Garwood M, Collins CM, Liu W, DelaBarre L, Adriany G, Andersen P, Merkle H, Goebel R, Smith MB, Ugurbil K. 7 T vs. 4T: RF power, homogeneity, and signal-to-noise comparison in head images. Magn Reson Med. 2001; 46:24–30. [PubMed: 11443707]

32. Abduljalil AM, Kangarlu A, Zhang X, Burgess RE, Robitaille PM. Acquisition of human multislice MR images at 8 Tesla. J Comput Assist Tomogr. 1999; 23:335–340. [PubMed: 10348433]

33. Yacoub E, Shmuel A, Pfeuffer J, Van De Moortele PF, Adriany G, Andersen P, Vaughan JT, Merkle H, Ugurbil K, Hu X. Imaging brain function in humans at 7 Tesla. Magn Reson Med. 2001; 45:588–594. [PubMed: 11283986]

34. Yang QX, Mao W, Wang J, Smith MB, Lei H, Zhang X, Ugurbil K, Chen W. Manipulation of image intensity distribution at 7.0 T: Passive RF shimming and focusing with dielectric materials. J Magn Reson Imaging. 2006; 24:197–202. [PubMed: 16755543]

35. Yang QX, Smith MB, Briggs RW, Rycyna RE. Microimaging at 14 tesla using GESEPI for removal of magnetic susceptibility artifacts in T(2)(*)-weighted image contrast. J Magn Reson. 1999; 141:1–6. [PubMed: 10527737]

36. Cunningham CH, Vigneron DB, Marjanska M, Chen AP, Xu D, Hurd RE, Kurhanewicz J, Garwood M, Pauly JM. Sequence design for magnetic resonance spectroscopic imaging of prostate cancer at 3 T. Magn Reson Med. 2005; 53:1033–1039. [PubMed: 15844147]

37. Kohler SJ, Yen Y, Wolber J, Chen AP, Albers MJ, Bok R, Zhang V, Tropp J, Nelson S, Vigneron DB, Kurhanewicz J, Hurd RE. In vivo 13 carbon metabolic imaging at 3T with hyperpolarized 13C-1-pyruvate. Magn Reson Med. 2007; 58:65–69. [PubMed: 17659629]

38. Cunningham CH, Chen AP, Albers MJ, Kurhanewicz J, Hurd RE, Yen YF, Pauly JM, Nelson SJ, Vigneron DB. Double spin-echo sequence for rapid spectroscopic imaging of hyperpolarized 13C. J Magn Reson. 2007; 187:357–362. [PubMed: 17562376]

39. Olsson LE, Chai CM, Axelsson O, Karlsson M, Golman K, Petersson JS. MR coronary angiography in pigs with intraarterial injections of a hyperpolarized 13C substance. Magn Reson Med. 2006; 55:731–737. [PubMed: 16538605]

40. Ishii M, Emami K, Kadlecek S, Petersson JS, Golman K, Vahdat V, Yu J, Cadman RV, MacDuffie-Woodburn J, Stephen M, Lipson DA, Rizi RR. Hyperpolarized 13C MRI of the pulmonary vasculature and parenchyma. Magn Reson Med. 2007; 57:459–463. [PubMed: 17326170]

41. Golman K, Zandt RI, Lerche M, Pehrson R, Ardenkjaer-Larsen JH. Metabolic imaging by hyperpolarized 13C magnetic resonance imaging for in vivo tumor diagnosis. Cancer Res. 2006; 66:10855–10860. [PubMed: 17108122]

42. Chew WM, Moseley ME, Nishimura MC, Hashimoto T, Pitts LH, James TL. A novel double-surface coil approach to phosphorus-31 spectroscopy: A study of hemispheric brain injury in the rat. Magn Reson Med. 1985; 2:567–575. [PubMed: 3880098]

43. Schnall MD, Subramanian VH, Leigh JS, Chance B. A new double-tuned probe for concurrent 1H and 31P NMR. J Magn Reson. 1985; 65:122–129.

44. Rath AR. Design and performance of a double-tuned bird-cage coil. J Magn Reson. 1990; 86:488–495.

45. Derby K, Tropp J, Hawryszko C. Design and evaluation of a novel dual-tuned resonator for spectroscopic imaging. J Magn Reson. 1990; 86:645–651.

46. Murphy-Boesch J, Srinivasan R, Carvajal L, Brown TR. Two configurations of the four-ring birdcage coil for 1H imaging and 1H-decoupled 31P spectroscopy of the human head. J Magn Reson B. 1994; 103:103–114. [PubMed: 8137076]

47. Vaughan JT, Hetherington HP, Otu JO, Pan JW, Pohost GM. High frequency volume coils for clinical NMR imaging and spectroscopy. Magn Reson Med. 1994; 32:206–218. [PubMed: 7968443]

48. Shen GX, Boada FE, Thulborn KR. Dual-frequency, dual-quadrature, birdcage RF coil design with identical B1 pattern for sodium and proton imaging of the human brain at 1.5 T. Magn Reson Med. 1997; 38:717–725. [PubMed: 9358445]

49. Shen GX, Wu JF, Boada FE, Thulborn KR. Experimentally verified, theoretical design of dual-tuned, low-pass birdcage radiofrequency resonators for magnetic resonance imaging and magnetic resonance spectroscopy of human brain at 3.0 Tesla. Magn Reson Med. 1999; 41:268–275. [PubMed: 10080273]

50. Wang C, Wu B, Xu D, Zhang X. A novel double-tuned head coil with 16 double-tuned elements for 7 T MRI/S," in. Proc 16th Annu Meeting ISMRM. 2008:2983.

51. Amari S, Ulug AM, Bornemann J, van Zijl PC, Barker PB. Multiple tuning of birdcage resonators. Magn Reson Med. 1997; 37:243–251. [PubMed: 9001149]

52. Xie Z, Zhang X. A novel dual-frequency volume coil using common mode/differential mode (CMDM) resonator at 7 T," in. Proc 16th Annu Meeting ISMRM. 2008:2985.

53. Xie Z, Vigneron DB, Zhang X. Dual-frequency coil design using common mode and differential mode (CMDM) technique for 1H/13C MRSI at 7 T," in. Proc 17th Annu Meeting ISMRM. 2009:2964.

54. Zhang X, Ugurbil K, Chen W. Microstrip RF surface coil design for extremely high-field MRI and spectroscopy. Magn Reson Med. 2001; 46:443–450. [PubMed: 11550234]

55. Lee RF, Westgate CR, Weiss RG, Newman DC, Bottomley PA. Planar strip array (PSA) for MRI. Magn Reson Med. 2001; 45:673–683. [PubMed: 11283996]

56. Zhang X, Ugurbil K, Chen W. A microstrip transmission line volume coil for human head MR imaging at 4T. J Magn Reson. 2003; 161:242–251. [PubMed: 12713976]

57. Zhang X, Ugurbil K, Sainati R, Chen W. An inverted-microstrip resonator for human head proton MR imaging at 7 tesla. IEEE Trans Biomed Eng. 2005; 52:495–504. [PubMed: 15759580]

58. Zhang X, Zhu XH, Chen W. Higher-order harmonic transmission-line RF coil design for MR applications. Magn Reson Med. 2005; 53:1234–1239. [PubMed: 15844152]

59. Adriany G, Van de Moortele PF, Wiesinger F, Moeller S, Strupp JP, Andersen P, Snyder C, Zhang X, Chen W, Pruessmann KP, Boesiger P, Vaughan T, Ugurbil K. Transmit and receive transmission line arrays for 7 Tesla parallel imaging. Magn Reson Med. 2005; 53:434–445. [PubMed: 15678527]

60. Wu B, Wang C, Krug R, Kelley DA, Xu D, Pang Y, Banerjee S, Vigneron DB, Nelson SJ, Majumdar S, Zhang X. 7 T human spine imaging arrays with adjustable inductive decoupling. IEEE Trans Biomed Eng. 2010; 57:397–403. [PubMed: 19709956]

61. Wu B, Wang C, Kelley DA, Xu D, Vigneron DB, Nelson SJ, Zhang X. Shielded microstrip array for 7 T human MR imaging. IEEE Trans Med Imaging. 2010; 29:179–184. [PubMed: 19822470]

62. Zhang, X.; Ugurbil, K.; Chen, W. Method and Apparatus for Magnetic Resonance Imaging and Spectroscopy Using Microstrip Transmission Line Coils. US Patent. 7023209. 2006.

63. Yee KS. Numerical solution of initial boundary value problems involving Maxwell equations in isotropic media. IEEE Trans Ant Propag. 1966; 14:302–307.

64. Collins CM, Smith MB. Calculations of B(1) distribution, SNR, and SAR for a surface coil adjacent to an anatomically-accurate human body model. Magn Reson Med. 2001; 45:692–699. [PubMed: 11283998]

65. Wang J, Yang QX, Zhang X, Collins CM, Smith MB, Zhu XH, Adriany G, Ugurbil K, Chen W. Polarization of the RF field in a human head at high field: A study with a quadrature surface coil at 7.0 T. Magn Reson Med. 2002; 48:362–369. [PubMed: 12210945]

66. Yang QX, Wang J, Zhang X, Collins CM, Smith MB, Liu H, Zhu XH, Vaughan JT, Ugurbil K, Chen W. Analysis of wave behavior in lossy dielectric samples at high field. Magn Reson Med. 2002; 47:982–989. [PubMed: 11979578]

67. Ong KC, Wen H, Chesnick AS, Duewell S, Jaffer FA, Balaban RS. Radiofrequency shielding of surface coils at 4.0 T. J Magn Reson Imaging. 1995; 5:773–777. [PubMed: 8748501]

68. Xie Z, Zhang X. A novel decoupling technique for non-overlapped microstrip array coil at 7 T MR imaging," in. Proc 16th Annu Meeting ISMRM. 2008:1068.

69. Xie Z, Zhang X. An 8-channel non-overlapped spinal cord array coil for 7 T MR imaging. Proc 16th Annu Meeting ISMRM. 2008:2974.
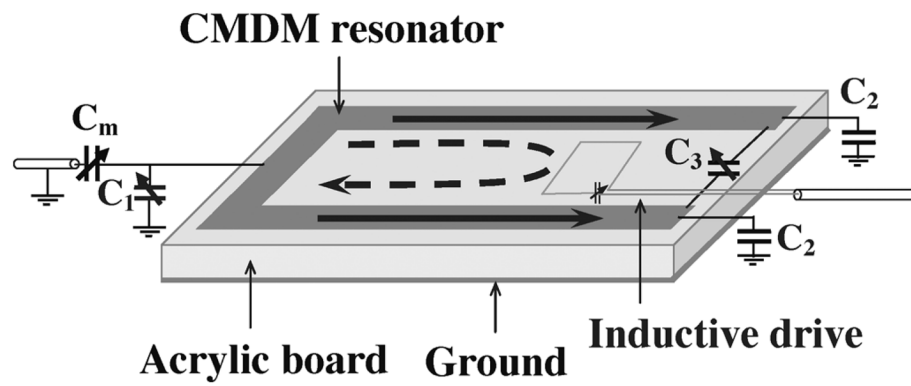
Fig. 1.
Diagram of the CMDM microstrip single surface coil. The solid line denotes the CM current, while the dashed line denotes the DM current. In this scheme the CM is driven capacitively while the DM is driven inductively.
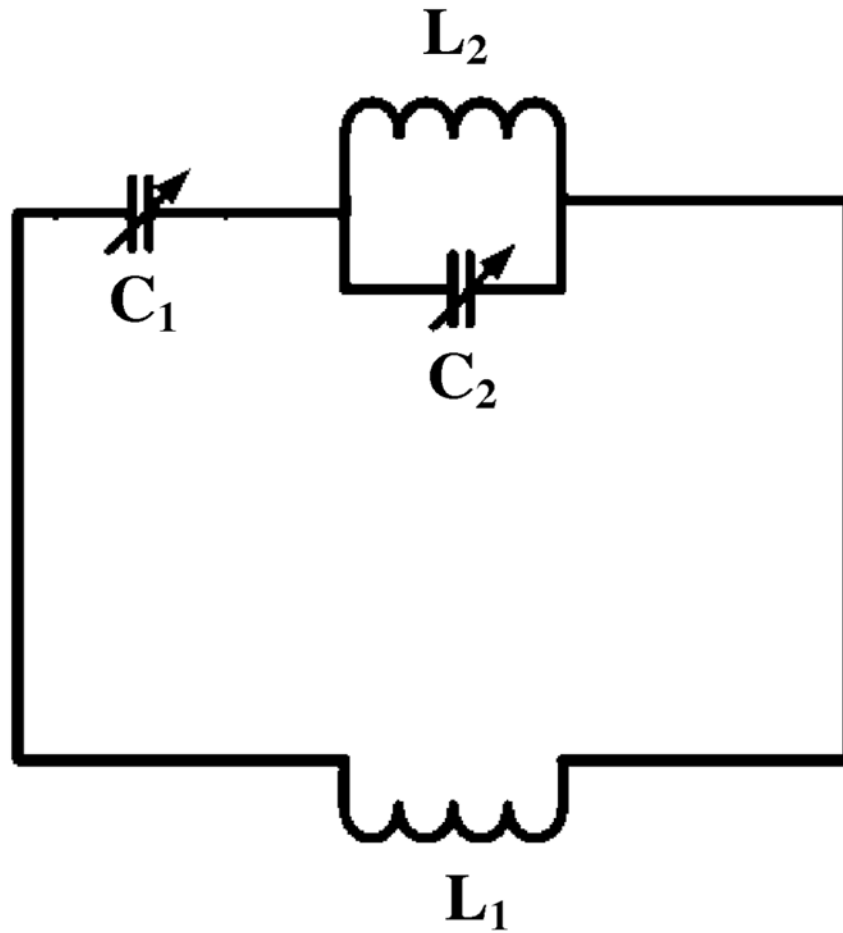
Fig. 2.
Equivalent circuit of the double-tuned two-pole coil for the comparison study. The trimmer capacitor C1 and C2 are used to perform frequency tuning for two frequencies. L1 is the equivalent inductance of the loop coil.
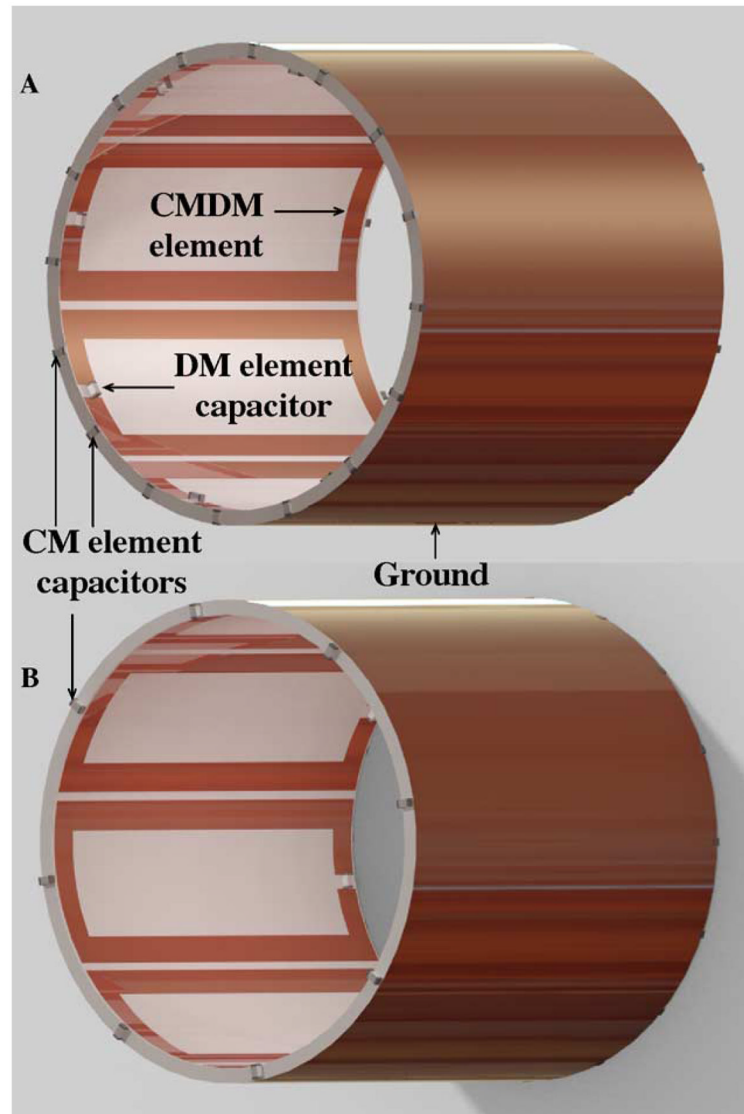
Fig. 3.
Diagram of the double-tuned CMDM microstrip volume coil implemented by using microstrip technology: views from (a) left sides and (b) right side.
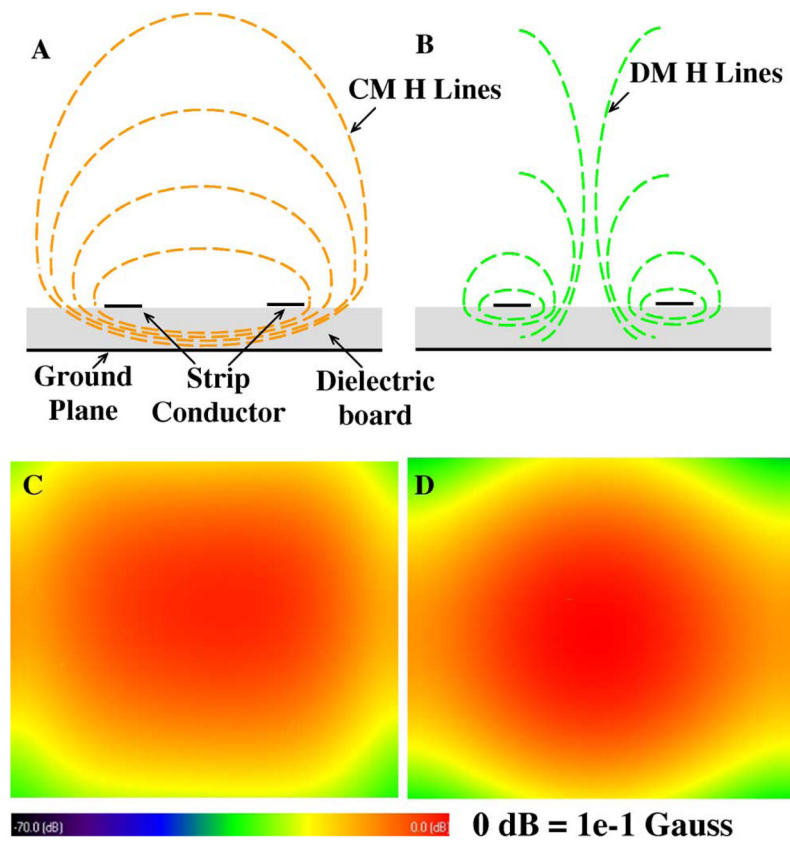
Fig. 4.
Magnetic field distributions of the (a) common mode and (b) differential mode of the CMDM microstrip double-tuned resonator. FDTD simulated B_1 maps (coronal) of (c) CM at 298.1 MHz and (d) DM at 75 MHz. The B_1 distributions of the common mode and differential mode are similar, helping B_0 shimming for low gamma nuclei.
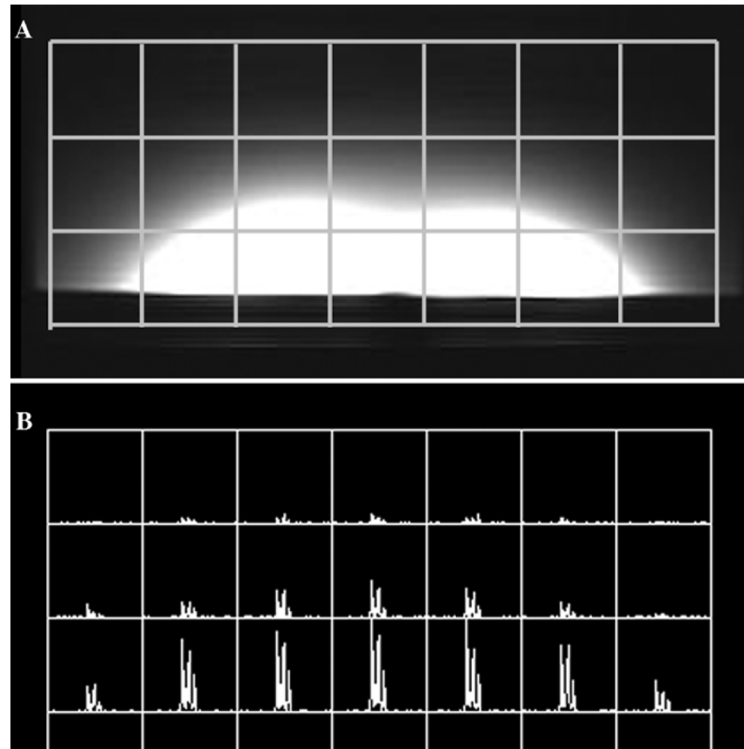
Fig. 5.
(a) ^{1}H SE image and (b) ^{13}C CSI of a corn oil phantom on the axial plane acquired using the CMDM single surface coil at 7T. These MR images show that the common mode and differential mode have similar B_1 distribution.
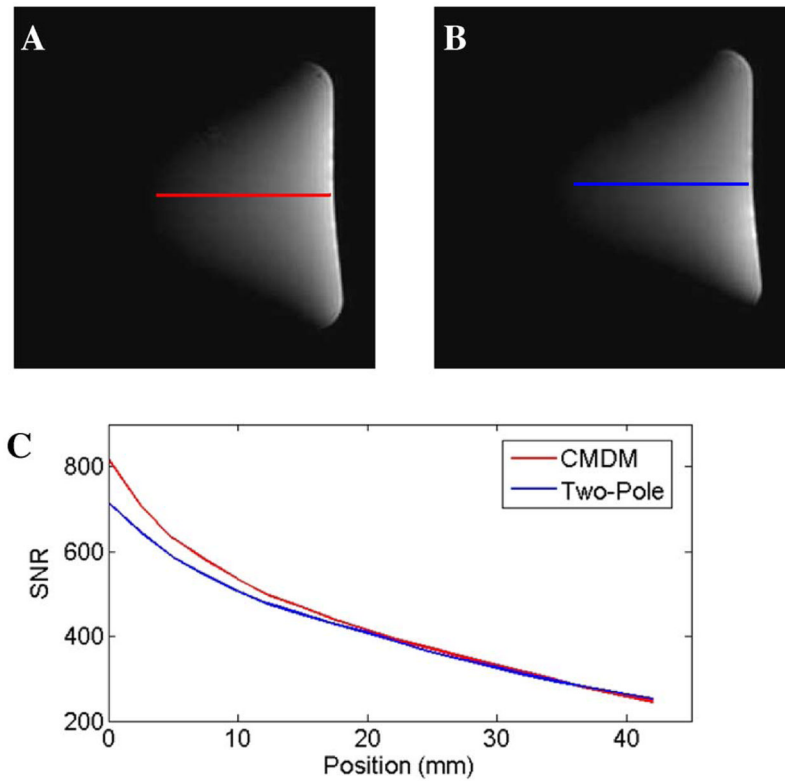
Fig. 6.
Results of the SNR comparison between the CMDM coil and the two-pole coil using a water phantom at 7T: (a) ^{1}H image of CMDM coil; (b) ^{1}H image of the two-pole coil; (c) SNR plot along the central line of the two images. The highest achievable SNR of the CMDM coil is 13% higher than that of the two-pole coil.
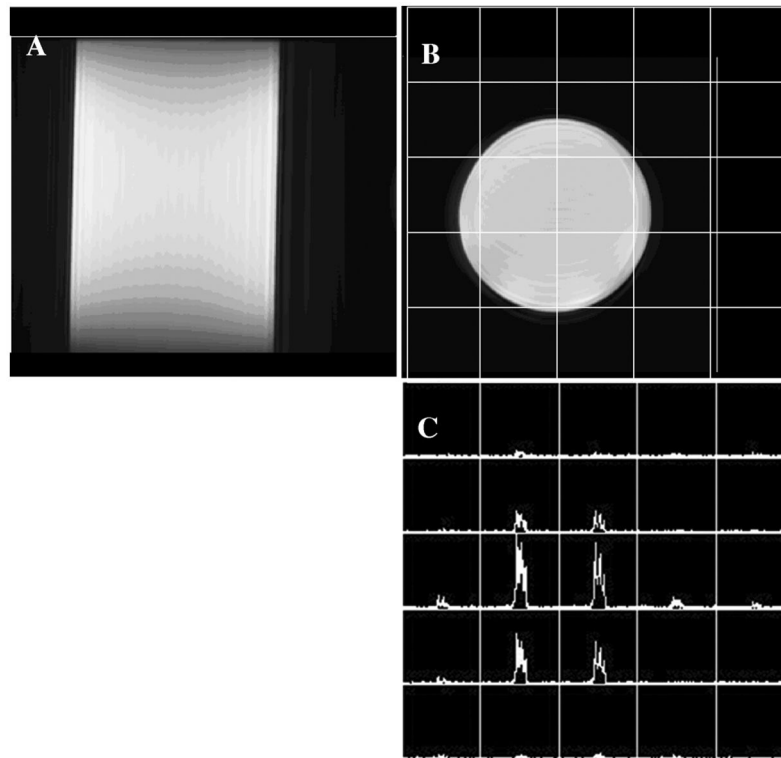
Fig. 7.
MR experiment results of a corn oil phantom using the CMDM double-tuned volume coil at 7T: (a) ^{1}H spin echo sagittal image; (b) ^{1}H axial image and (c) ^{13}C CSI spectroscopic image on axial plane acquired with natural abundance. The ^{1}H images demonstrate the fairly homogeneous axial B_1 distribution in the imaging area at the high frequency of ~300 MHz. In the ^{13}C CSI result, given the partial volume effect, the ^{13}C channel of this dual-tuned volume coil has a right behavior in terms of resonant mode and uniform field distributions at 75 MHz.
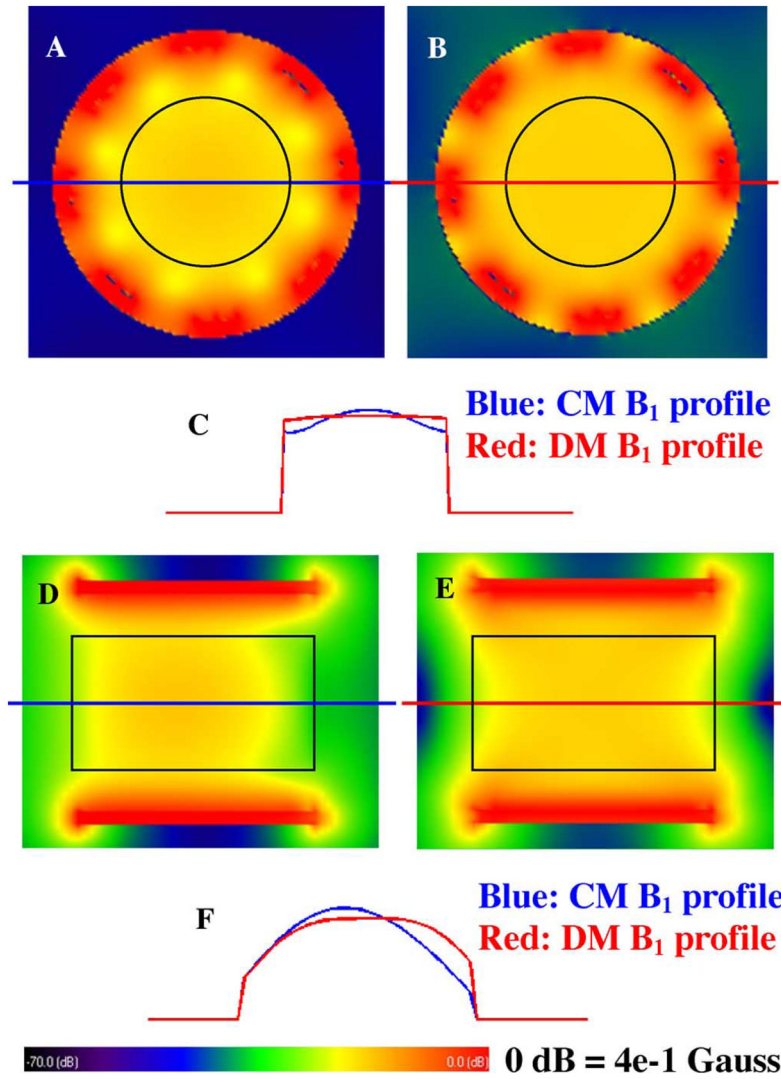
Fig. 8.
FDTD simulation results of the B_1 distribution of the double-tuned CMDM volume coil at 7T in the loaded case. The black circles in (a) and (b) and black rectangles in (d) and (e) denote the phantom position. (a) Axial plane B_1 distribution of the common mode channel for [1]H. (b) Axial plane B_1 distribution of the differential mode channel for [13]C. (c) 1-D plot of the axial plane B_1 distribution, blue line and red line denote the ^{1}H and ^{13}C, respectively. (d), (e) Sagittal plane B_1 distributions of the common mode channel for ^{1}H and the differential mode channel for [13]C. (f) 1-D profile of the sagittal plane B_1 distribution, blue line and red line denote the ^{1}H and ^{13}C respectively. It is shown that for ^{13}C channel with the differential mode operating at 75 MHz, homogeneous B_1 field distribution was obtained in both axial and sagittal directions, while for ^{1}H channel with the common mode operating at 300 MHz, although "dielectric resonance" effects at ultrahigh fields distort the B_1 field, a fairly homogeneous B_1 distribution was still obtained in this case.

TABLE I

Performance Comparison Between the CMDM Coil and the Two-Pole Coil in Terms of Q-Values and the Electromagnetic Isolation Between Channels in Both Unloaded and Loaded Cases. In All the Measurements, the Coil's Input Impedance Was Well Matched to the System at 50 Ω

| | | CMDM | | Two-pole | |
		C13	H1	C13	H1
Unloaded	Q value	300	246	178	185
	S21(dB)	−50	−45	−15	−22
Loaded	Q value	150	52	66	50
	S21(dB)	−44	−44	−13	−21